1 **Generating immunogenomic data-guided virtual patients using a QSP model to predict response of**
2 **advanced NSCLC to PD-L1 inhibition**
3

4 **Authors:** Hanwen Wang[1]*, Theinmozhi Arulraj[1], Holly Kimko[2], Aleksander S. Popel[1,3]
5

6 **Affiliations:**

7 [1] Department of Biomedical Engineering, Johns Hopkins University School of Medicine, Baltimore, MD
8 21205, USA

9 [2] Clinical Pharmacology & Quantitative Pharmacology, AstraZeneca, Gaithersburg, MD, USA

10 [3] Department of Oncology, and the Sidney Kimmel Comprehensive Cancer Center, Johns Hopkins
11 University School of Medicine, Baltimore, MD 21205, USA

12
13 ***Corresponding author. Email:** hwang163@jhmi.edu

14
15 **Abstract:**

16 Generating realistic virtual patients from a limited amount of patient data is one of the major challenges
17 for quantitative systems pharmacology modeling in immuno-oncology. Quantitative systems
18 pharmacology (QSP) is a mathematical modeling methodology that integrates mechanistic knowledge of
19 biological systems to investigate dynamics in a whole system during disease progression and drug
20 treatment. In the present analysis, we parameterized our previously published QSP model of the cancer-
21 immunity cycle to non-small cell lung cancer (NSCLC) and generated a virtual patient cohort to predict
22 clinical response to PD-L1 inhibition in NSCLC. The virtual patient generation was guided by
23 immunogenomic data from iAtlas portal and population pharmacokinetic data of durvalumab, a PD-L1
24 inhibitor. With virtual patients generated following the immunogenomic data distribution, our model
25 predicted a response rate of 18.6% (95% bootstrap confidence interval: 13.3-24.2%) and identified
26 CD8/Treg ratio as a potential predictive biomarker in addition to PD-L1 expression and tumor mutational
27 burden. We demonstrated that omics data served as a reliable resource for virtual patient generation
28 techniques in immuno-oncology using QSP models.
29
30

31 **INTRODUCTION**

32 Lung cancer is the top leading cause of cancer death in the U.S. with 130,180 estimated deaths in 2022 *(1)*.
33 Non-small cell lung cancer (NSCLC) is the most common subtype of lung cancer, which accounts for
34 about 84% of total lung cancer cases *(2)*. Since 2015, immune checkpoint inhibitors targeting
35 programmed cell death protein (death-ligand) 1 [PD-(L)1] and cytotoxic T-lymphocyte antigen-4 (CTLA-
36 4) have begun to receive approval from the U.S. Food and Drug Administration (FDA) for advanced
37 NSCLC. For patients without actionable mutations [i.e., epidermal growth factor receptor (EGFR) and
38 anaplastic lymphoma kinase (ALK)], different immune checkpoint inhibitors are recommended in single-
39 agent or dual immunotherapy, or in combination with chemotherapy or bevacizumab, an anti-VEGF
40 antibody, based on PD-L1 expression level on tumor cells *(3)*. PD-L1 expression, as a regulator of
41 antitumor response, an indicator of T cell infiltration into the tumor, and the target of immune checkpoint
42 inhibitors, has been widely used as a predictive biomarker for immunotherapy in advanced NSCLC *(4)*.
43 Although immunotherapy has significantly improved the overall survival rate in advanced NSCLC when
44 compared to conventional treatments, less than half of the patients respond (including those with >50%
45 PD-L1 expression on tumor cells), and the 3-year survival rate is significantly lower in patients without
46 actionable mutations *(5)*. Due to the low prevalence of actionable mutations *(6)*, novel combination
47 regimens that involve immune checkpoint inhibitors are under investigation in clinical trials *(3)*.
48

1

49   In conjunction with the clinical effort, quantitative systems pharmacology (QSP) models have been
50   developed in the past few years, aiming to predict clinical benefits of treatment of interest in complex
51   diseases like NSCLC. QSP integrates mechanistic knowledge from multiple disciplines, such as systems
52   biology, (patho)physiology, and pharmacology, and investigates dynamic behavior of a system as a whole
53   *(7)*. Particularly in immuno-oncology, increasing number of QSP models was developed to study drug
54   exposure-efficacy and exposure-toxicity relationships, predict efficacy, and identify predictive biomarkers
55   for newly discovered drugs, including T cell engagers, immune checkpoint inhibitors (ICIs), and chimeric
56   antigen receptor (CAR) T cells *(8)*. The main goal is to assist drug and clinical trial designs, such as target
57   and dose optimization, and to reduce the cost and time in drug development *(9, 10)*. Among these efforts,
58   our previously developed QSP platform, QSP-IO, has been applied to simulate tumor response to ICIs
59   and their combinations with other types of treatment in early-stage NSCLC *(11, 12)*, breast cancer *(13–*
60   *15)*, colorectal cancer *(16, 17)*, and hepatocellular carcinoma *(18)*. Although recent QSP models provide
61   reliable efficacy predictions for clinical trials at the population level, one of the major challenges remains
62   in virtual patient generation, which aims to generate virtual patient cohorts that represent the
63   interindividual variabilities observed in real-world data while falling within the physiologically plausible
64   ranges *(15)*.

65

66   Although methods have been proposed to guide virtual patient generation, they have not been widely
67   applied to large-scale models like QSP *(19, 20)*. The focus of this study is therefore to investigate the
68   performance of published virtual patient generation methods when integrated with our latest QSP-IO
69   platform *(15)*. Specifically, we applied two virtual patient generation methods: 1) probability of inclusion
70   *(21)* to select virtual patients that statistically match patient data from the Cancer Research Institute (CRI)
71   iAtlas, a platform storing results from immunogenomic analyses of TCGA data *(22)*; and 2) compressed
72   latent parameterization *(23)* to generate pharmacokinetic (PK) parameters based on pseudo-patient level
73   data from population PK analysis of durvalumab, a PD-L1 inhibitor. For model validation, we first
74   predicted the objective response rate of the generated virtual patients to durvalumab to compare with
75   results from Study 1108 (NCT01693562), a phase 1/2 clinical trial in advanced NSCLC *(24)*. In addition,
76   we validated model-predicted immune cell densities against results from a digital pathology analysis,
77   which is a quantitative analysis of histological images that provides spatial densities of immune markers
78   of interest, such as CD4, CD8, and FoxP3, in different tumor regions *(25–29)*.

79

80   **RESULTS**

81   *Model parameterization*

82   Figure 1 illustrates the workflow of the present analysis. We utilized our previously developed QSP
83   platform *(15)* that describes the cancer-immunity cycle *(30)* and recalibrated the cancer-type specific
84   parameters using experimental and clinical data on NSCLC. Table 1 lists the recalibrated parameters with
85   the data we used to estimate their values. As we aim to simulate a phase 1/2 clinical trial of durvalumab
86   that enrolled patients with stage III NSCLC, data on stage III NSCLC were preferentially used when
87   available. Overall, the model involves four main compartments: central, peripheral, tumor, and tumor-
88   draining lymph node. Ten modules were incorporated to investigate dynamics of cellular and molecular
89   species, including cancer cells, T cells (i.e., effector, helper, and regulatory T cells), immune checkpoints,
90   and durvalumab, in their corresponding compartments. Since majority of the clinical data for virtual
91   patient generation and model validation (e.g., CD8 and CD4 T cell density) were collected from tumor
92   samples, the model was best trained to describe immune cell dynamics in the tumor compartment, which
93   is therefore the focus of the following analyses. With the recalibrated model, we first generated 30,000
94   plausible patients, 629 of which were selected to form a virtual patient cohort. The selection process was
95   guided by immune cell subset ratios (i.e., M1/M2, CD8/Treg, and CD8/CD4) estimated from
96   immunogenomic analysis, as described below in Methods.

Figure 1. Paradigm of immunogenomic data-guided virtual patient generation and in silico clinical trial simulation using a mechanistic quantitative systems pharmacology model. The model is comprised of four compartments: central, peripheral, tumor, and tumor-draining lymph node, which together describe the cancer-immunity cycle. nT, naïve T cell; aT, activated T cell; NO, nitric oxide; Arg-I, arginase I; Treg, regulatory T cell; Teff, effector T cell; Th, helper T cell; Mac, macrophage; mAPC, mature antigen presenting cell. Cytokine degradation and cellular clearance are omitted in the figure.

Table 1. Non-small cell lung cancer (NSCLC)-specific parameters in the quantitative systems pharmacology model. MHC, major histocompatibility complex.

Parameter	Value	Unit	Description
k_C1_growth	0.007	1/day	Rate of cancer cell proliferation in clone $C1$, estimated by the clinically observed tumor volume doubling time *(31)*.
C_max	1.5e11	cell	Maximal tumor carrying capacity corresponding to a maximal tumor size of 10 cm.
γ_T	5%	dimensionless	Volume fraction of vascular space in NSCLC tumor estimated by dividing pulmonary vessel volume *(32)* by the total lung tissue volume *(33)* and assuming vascular space in NSCLC is about 29% of that in normal lung tissue *(34)*.
V_e	75%	dimensionless	Volume fraction of intracellular space in NSCLC tumor *(35)*.
T_PD1	176	molecule/μm^2	Average PD-1 density on T cells in the tumor *(15)*.
C_PDL1	250	molecule/μm^2	Average baseline PD-L1 density on cancer cells/antigen-presenting cells in the tumor in absence of IFNγ assuming it is 6-fold lower than the maximal density *(15)*.
C_CD47	100	molecule/μm^2	Average CD47 density on cancer cells in the tumor estimated based on the experimentally observed increase of phagocytosis index when CD47-SIRP interaction is blocked in NSCLC *(36)*.
n_T1_clones	92	dimensionless	Number of NSCLC-specific T cell clones *(11)* that can recognize cancer cell clone $C1$.
n_T0_clones	100	dimensionless	Number of tumor-associated self-antigen-specific T cell clones *(11)* that activate regulatory T cells.
k_P1_d1	40	nmol/L	Average binding affinity between NSCLC neoantigens and MHC molecules *(11)*.
k_MDSC_rec	2,000	cell/(mL*day)	Rate of MDSC recruitment into the tumor estimated by digital pathology analysis of NSCLC tumor samples *(37)*.
k_Mac_rec	200,000	cell/(mL*day)	Rate of macrophage recruitment into the tumor estimated by digital pathology analysis of NSCLC tumor samples *(38)*.
k_M1_pol	0.02	1/day	Rate of M2-to-M1 macrophage polarization estimated by M1/M2 ratios calculated from TCGA data analysis *(22, 39)*.
$nLNs$	21	dimensionless	Number of tumor-draining lymph node surrounding the tumor *(11)*.
D_cell	16.9	μm	Diameter of a single NSCLC cell *(11)*.
$initial\_tumour\_size$	3.7	cm	Pre-treatment tumor diameter estimated by the measured target lesion sizes at diagnosis in the OAK trial *(40, 41)*.

4

108   *Virtual patient generation*

109   We first confirmed that the virtual patient cohort statistically matched the immunogenomic data that
110   guided the selection process. Figure 2A shows the estimated probability densities of the three immune
111   subset ratios in: 1) the plausible patients, 2) the final virtual patient cohort, and 3) the immunogenomic
112   dataset from iAtlas portal *(22)*. We also compared the distributions of the three ratios between the
113   observed data and the virtual patients in Figure 2B. When comparing the distributions using Kolmogorov-
114   Smirnov tests, the test statistics were 0.07, 0.06, and 0.06 with p-values of 0.30, 0.51, and 0.44, indicating
115   that the virtual patient's distributions were not statistically different from those of the immunogenomic
116   data. Also shown in Figure 2A, the ranges of immune subset ratios in the plausible patients were wider
117   than that in the immunogenomic data, which were narrowed by the selection process to generate the
118   virtual patient population that better fitted to the data. Here, we use immune subset ratios instead of the
119   proportions of immune cells in leukocytes as reported in iAtlas database because the proportions do not
120   directly correspond to our model outputs, where immune cell densities are calculated in cells per cubic
121   milliliter of tumor. In addition, we only selected data on M1/M2 macrophages, CD8, CD4, and regulatory
122   T cells because other cellular types on the database (e.g., natural killer cells, B cells) were not explicitly
123   represented in the current model.
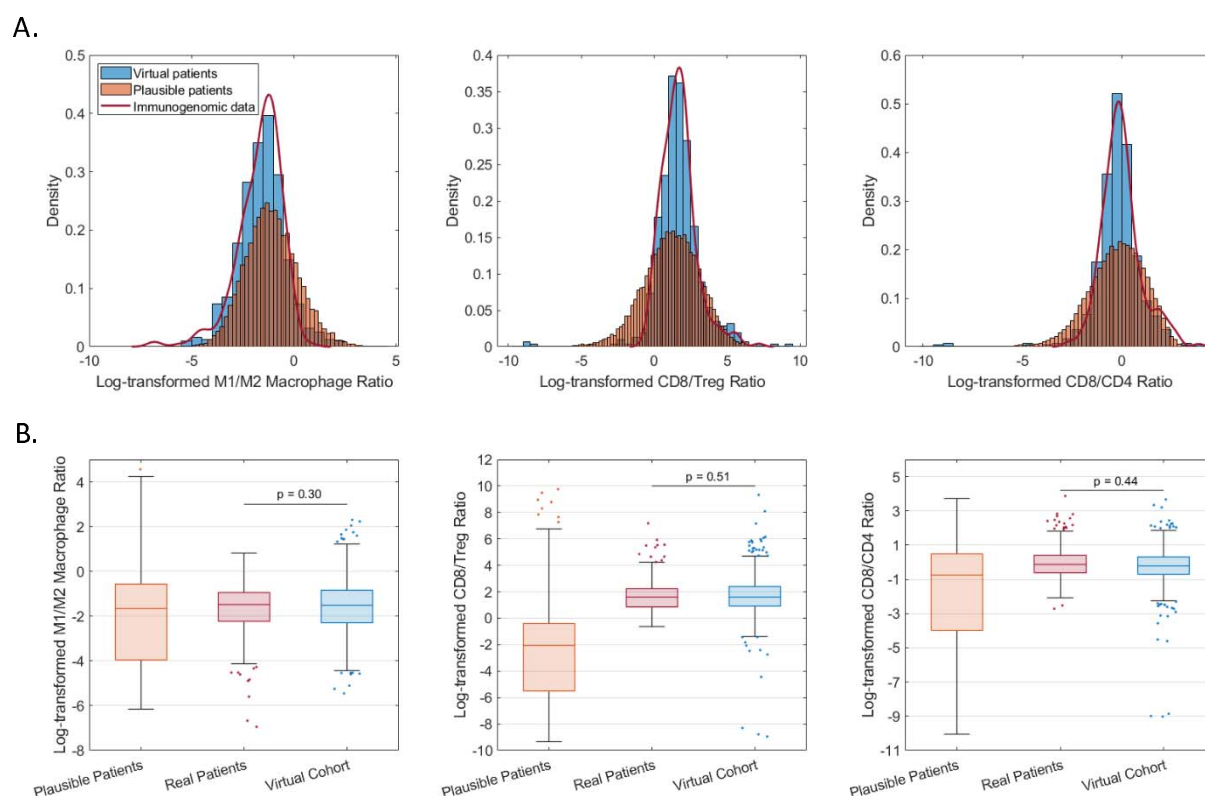124
125

A.

B.

126
127   **Figure 2. Probability density (A) and distribution (B) of model-predicted pre-treatment immune
128   cell subset ratios in the virtual patient cohort compared with that calculated from immunogenomic
129   data analysis.** In the top panels, red lines represent the estimated probability density functions from
130   immunogenomic data analysis; orange bars represent probability densities in the randomly generated
131   plausible patient population; blue bars represent probability densities in the selected virtual patient cohort.
132   In the bottom panels, 25th, 50th, and 75th percentiles are encoded by box plots with whiskers that define 1.5
133   times the interquartile range away from the bottom or top of the box. Natural-log transformation was
134   performed for the immune cell subset ratios during virtual patient generation.
135
136

5

137 Next, we validated the virtual patient cohort by comparing other pre-treatment characteristics of the
138 virtual patients with observed data from clinical analyses. Figure 3 shows the probability densities of the
139 pre-treatment tumor size, tumor doubling time, densities of CD8, CD4, Treg, and tumor-associated
140 macrophages (TAMs), myeloid-derived suppressor cells (MDSCs), and PD-L1 expression in the tumor.
141 The median tumor size is 3.7 cm with a range between 1.5 and 9.9 cm, which is consistent with the
142 measurement from the OAK trial for stage IIIB/IV NSCLC *(40, 41)*. The tumor volume doubling time
143 (TVDT) of virtual patients was calculated by $TVDT = \delta t \cdot \log 2 /(\log V_{t2} - \log V_{t1})$. δt is the time
144 interval between two CT scans that are usually performed at diagnosis and at the beginning of the
145 treatment. V_{t1} and V_{t2} are the measured tumor volumes at the two time points. Assuming a δt of 8 weeks,
146 we estimated the mean TVDT to be 113 days with a median of 89 days in the virtual patients, which
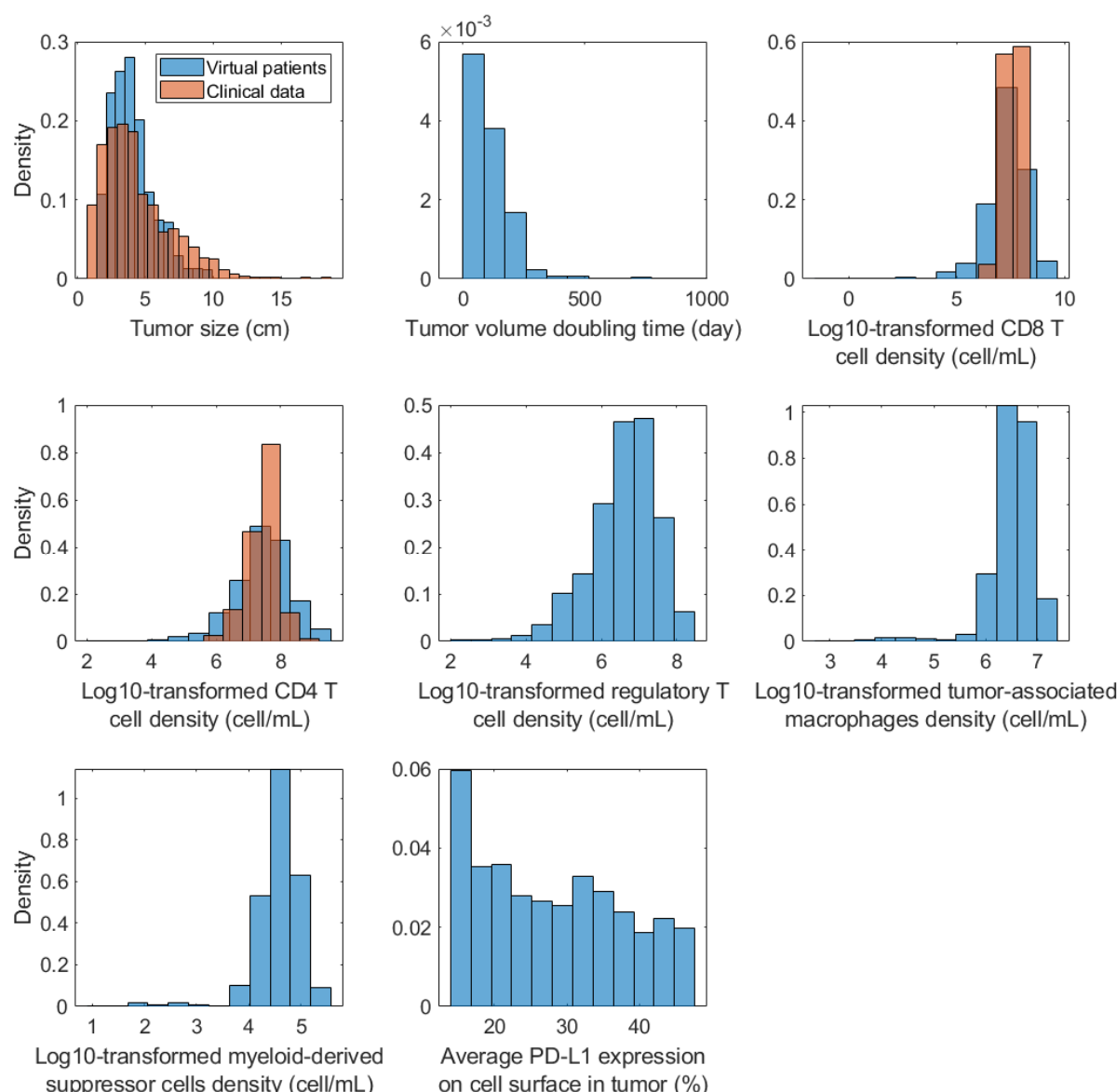147 aligned with clinically measured TVDT of stage III NSCLC *(31)*.
148
149

150
151 **Figure 3. Probability density of model-predicted pre-treatment variable distribution in the virtual**
152 **patient cohort.** Clinical data on tumor size were from the OAK trial *(40, 41)*. CD8 and CD4 T cell

6

153 densities in NSCLC tumor were obtained from Kilvaer et al. *(42)*. Average PD-L1 expressions on cell
154 surface were estimated by dividing the model-predicted average PD-L1 density across all cells in the
155 tumor by a theoretical maximal PD-L1 density of 1,770 molecules/μm^2.
156
157 The median densities of CD8, CD4, Treg, TAMs, and MDSCs were 2.6e7, 3.2e7, 5.4e6, 3.7e6 and 4.2e4
158 cells/mL in the tumor, which were in agreement with multiple digital pathology analyses *(37, 38, 43–45)*.
159 In Figure 3 and Supplementary Figure 1, we compared the distributions of CD8 and CD4 density between
160 virtual patients and clinical data from patients with stage III NSCLC, which were obtained from Kilvaer
161 et al. *(42)*. The conversion from a 2-D density from digital pathology analyses to the 3-D density was
162 performed using equations presented in Mi et al. *(26)*. Notably, the ranges of CD8 and CD4 T cell
163 densities in the virtual patients were wider than that in the clinical data, which was due to the inherent
164 uncertainty resulted from model parameterization and virtual patient generation. Nonetheless, the model-
165 predicted T cell subset densities likely fell within the physiologically reasonable ranges, as the
166 proportions of CD8 and CD4 T cells ranged from 0% to 40% in iAtlas data (zeros were removed when
167 calculating immune subset ratios to avoid singularities). Overall, the virtual patient cohort shows
168 resemblance to real patient populations observed in clinical analyses of NSCLC.
169
170 *Variability in pharmacokinetic parameters*

171 According to the population PK (popPK) study of durvalumab, drug exposure can be affected by
172 characteristics like body weight, serum albumin, and soluble PD-L1 level *(46)*. Although most of these
173 clinically measured characteristics are not present in the QSP model, the covariate effect on PK was
174 included during reproduction of the PK data to be fitted with the QSP model. Since immunogenomic data
175 used to select virtual patients above were not coupled with PK-related data, we independently generated
176 PK parameters for the virtual patients via compressed latent parametrization *(23)*. This optimization
177 method added an additional term to the mean-squared-error cost function to limit deviations from the
178 group-average model (see Methods), and thus allowed us to maintain the PK parameters within a
179 physiologically reasonable range.
180
181 Figure 4A shows the six PK parameters in the QSP model that were randomly generated to reflect the
182 variability in PK of durvalumab. The median capillary filtration rate was 5.6e-6 L/s, which is in
183 agreement with our previous analysis of the relationship between experimentally observed permeability
184 and the molecular size of durvalumab *(47)*. The median blood volume in the virtual patients is 5.8 liters,
185 which agrees with the observed body weight distribution in the popPK study, given that the blood volume
186 is approximately 70 mL/kg in adult humans. Further, the volume fraction of interstitial space in peripheral
187 tissues available to durvalumab ranges from 3.5 to 7.9%, consistent with estimation in our previous study
188 *(48)*. The clearance rates (both linear and non-linear) and Michaelis-Menten constant for non-linear
189 clearance are also consistent with the estimated values in the popPK study *(46)*. The QSP model-predicted
190 serum durvalumab concentration in the virtual patients is shown with clinically measured mean and
191 standard deviation in Figure 4B. Consistent with clinical observations, durvalumab concentration reached
192 steady state at approximately week 16 *(49)*. Model-predicted peak and trough concentrations after the first
193 dose and the trough concentration at steady state were comparable to clinical measurements from Study
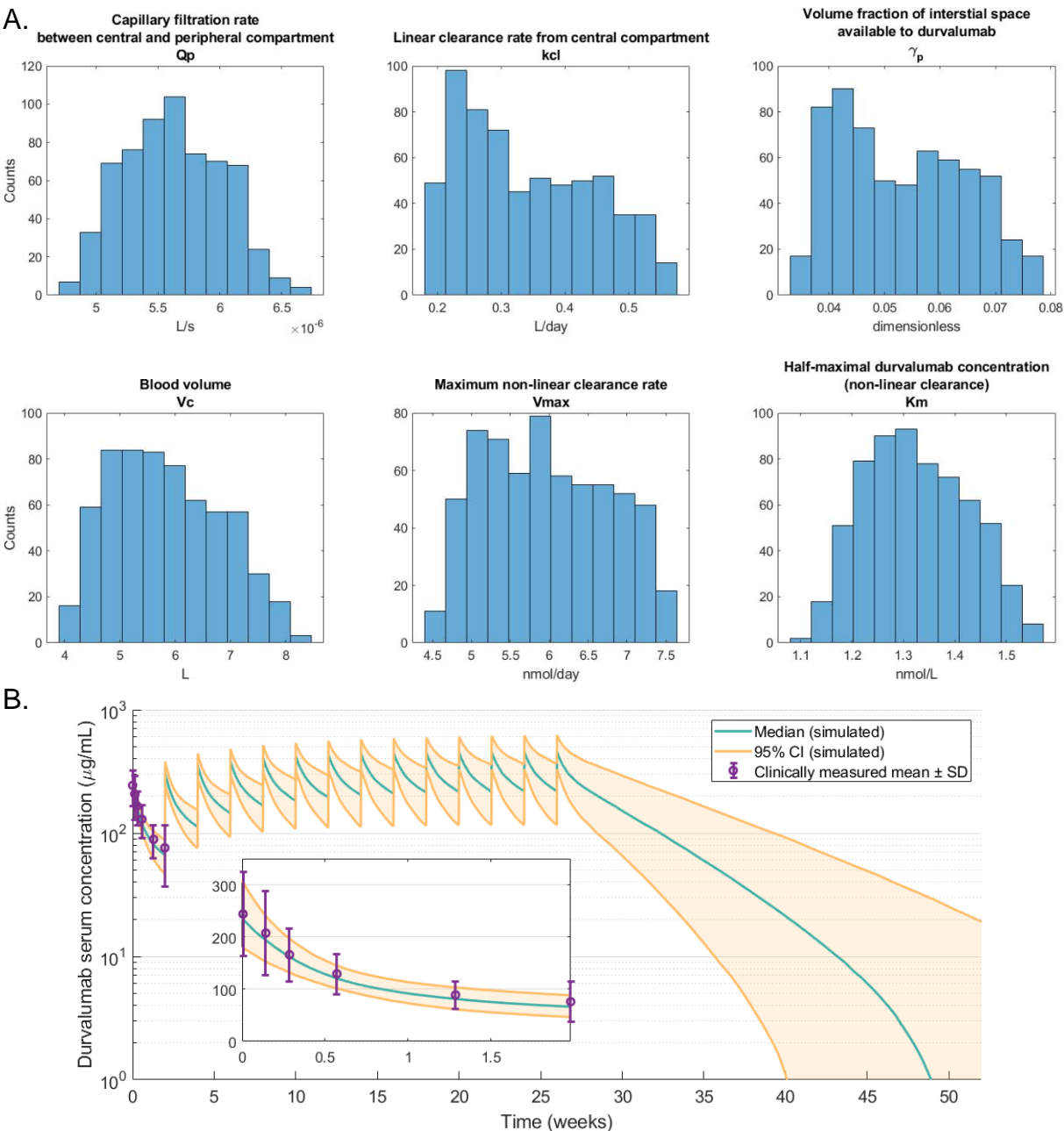194 1108 and the ATLANTIC trial (Supplementary Table 1) *(49)*.

7

Figure 4. (A) Distribution of fitted pharmacokinetic parameter values in the quantitative systems pharmacology model and (B) model-predicted durvalumab serum concentration following a flat-dosing regimen of 750 mg every 2 weeks (Q2W). Green line represents the median model prediction; Orange lines represent the 5th and 95th percentiles.

Predicting tumor dynamics during PD-L1 inhibition

With the PK parameters randomly generated from the latent space, we simulated PD-L1 inhibition in the virtual patient cohort. Durvalumab was administered with 750 mg flat doses every 2 weeks (Q2W) once each virtual patient reached the preset initial tumor diameter ranging from 1.5 to 9.9 cm (Figure 3). Tumor response to the treatment was analyzed in two virtual patient subgroups divided based on PD-L1 expression in the tumor with a threshold of 25%, which corresponds to the threshold used in Study 1108

8

209   *(24)*. In the clinical setting, PD-L1 expression is the percentage of tumor cells that exhibit membrane
210   staining by the reagent *(24)*. According to our model prediction, the majority of the cells that express PD-
211   L1 in the tumor were cancer cells, and since the PD-L1 density in the model was defined as the average
212   PD-L1 level on cells in the tumor, we approximated the PD-L1 expression by dividing the model-
213   predicted PD-L1 density by a theoretical maximum level of 1,770 molecules/μm^2. The maximum level
214   was estimated by the in vitro measurements of PD-L1 density on mature dendritic cells *(50, 51)*. Due to
215   the lack of data on PD-L1 expression in NSCLC tumors, we estimated the average baseline PD-L1
216   expression (Table 1) so that the proportion of virtual patients that fell within each subgroup matched that
217   reported by Study 1108 *(24)*.

219   Figure 5 shows the percentage change of tumor size and the best overall tumor size change in the two
220   patient subgroups. Although the model predicted a faster median tumor growth for non-responders with a
221   PD-L1-high tumor, responders in the PD-L1-high group showed a faster median tumor size reduction
222   during early stage of the treatment. Specifically, 22.6% of the responders in the PD-L1-high group
223   responded by week 6, as opposed to 6.1% in the PD-L1-low group. According to RECIST 1.1, the model
224   predicted an objective response rate (ORR) of 18.6% with a 95% bootstrap confidence interval of (13.3,
225   24.2)% in the virtual patient cohort. In PD-L1-high and -low groups, ORRs were predicted to be 23.8
226   (16.3, 32.7)% and 12.0 (5.5, 20.2)%, respectively. The increase in ORR in the PD-L1-high group was
227   potentially due to the positive correlation between PD-L1 expression and T cell infiltration
228   (Supplementary Figure 2), which was also clinically observed *(43)*. Comparing to the model-predicted
229   ORRs, the clinically reported ORRs in Study 1108 (21.8% and 6.4% for PD-L1 high vs. low) fall within
230   the model-predicted 95% confidence intervals, while the difference in predicted ORRs between the two
231   subgroups is narrower than that in the clinical trial. Our ORR prediction may be further improved by
232   including new lesion formation in the model, since a large portion of the patients with low PD-L1
233   expression in Study 1108, despite having a >30% tumor size reduction, was categorized as non-responder
234   due to detection of new lesion(s) *(24)*.

236   To further examine the performance of the virtual patient generation method, we simulated the same dose
237   regimen of durvalumab in virtual patients selected by different combinations of immunogenomic data.
238   Supplementary Table 2 shows that model-predicted ORRs were similar among virtual patient populations
239   selected by any data combinations. This is likely because the parameter distributions that generate
240   plausible patients were already manually calibrated to NSCLC data (see Methods). However, when we
241   selected virtual patients by data on lung adenocarcinoma (LUAD) or lung squamous cell carcinoma
242   (LUSD) separately, the model predicted higher ORR in LUSC with a median CD8/Treg ratio almost
243   twice as high as that in LUAD, which aligned with clinical findings *(52)*. This observation suggests that
244   the virtual patient generation method is capable of generating virtual patient populations that fit to
245   particular patient subgroups while reducing the inherent uncertainty (as seen above in Figure 2A).

247   Next, we investigated the correlations between response status and PK variables, including the peak
248   (C_{max}), trough (C_{min}) durvalumab concentration, and area under concentration curve (AUC) at early time
249   points and steady state (week 16), as well as drug accumulation indices. Supplementary Figure 3 shows
250   that the peak durvalumab concentration and AUC from day 0-14, as well as the peak concentration at
251   steady state, were significantly higher in responders. We further divided the virtual patient into 5
252   subgroups with increasing level of each PK variable and calculated the ORR of each subgroup in
253   Supplementary Figure 4. Interestingly, the ORR increased as C_{max} and AUC of the first dose (day 0-14)
254   increased, with about a 14% difference in ORR between the 2 subgroups with the highest and the lowest
255   level of $C_{max,1}$ or AUC_{0-14}. Nonetheless, a reverse trend, even though non-significant, was observed
256   between ORR and $C_{max,1}$ in patients with urothelial carcinoma from Study 1108 *(49)*.
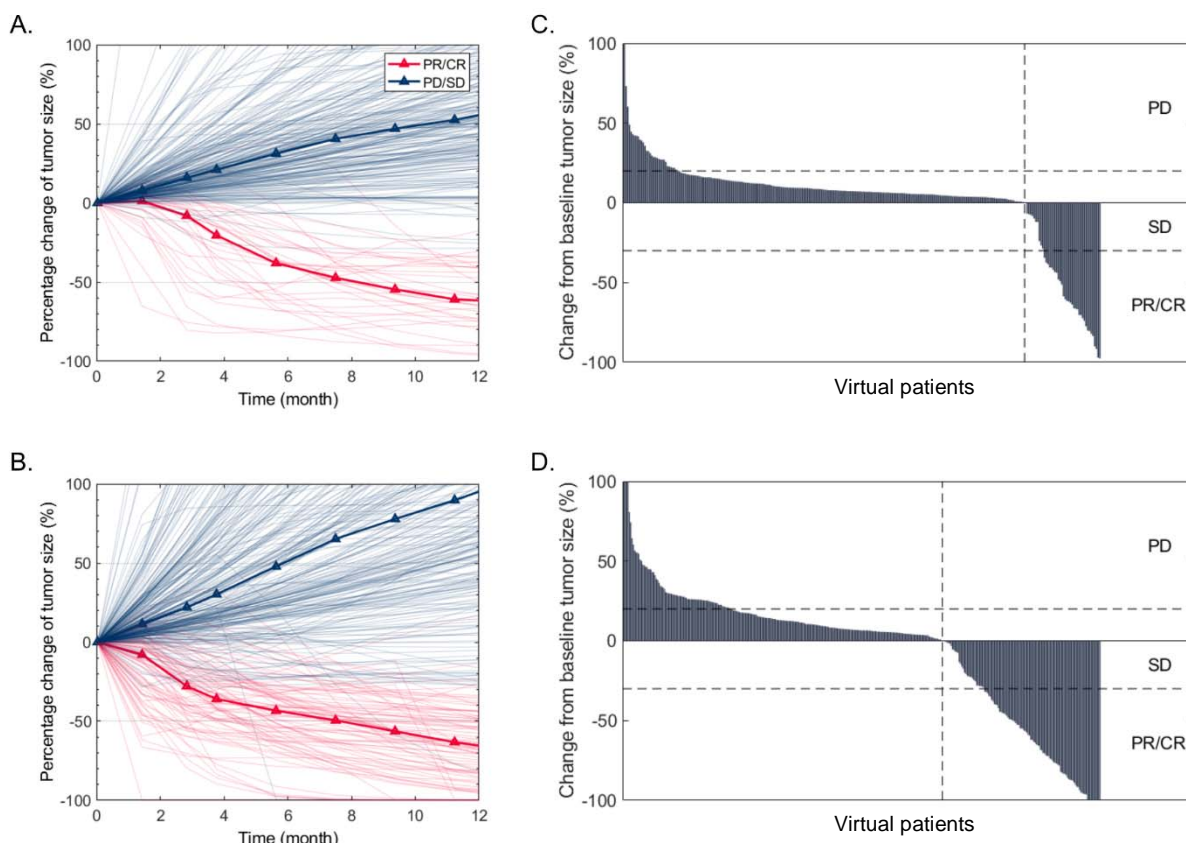
257

9

Figure 5. Percentage change in tumor size (A,B) and the best overall tumor size change (C,D) in PD-L1-low (A,C; N=276) and PD-L1-high (B,D; N=353) virtual patients during in silico clinical trials of durvalumab. R, responders; NR, non-responders; PD, progressive disease; SD stable disease; PR/CR, partial/complete response.

To investigate the performance of potential predictive biomarkers in NSCLC, we compared their distributions between responders and non-responders from the overall virtual patient cohort. Figure 6 shows that responders have significantly higher CD8/4 T cells, PD-L1 level, CD8/Treg and CD8/CD4 ratios, number of NSCLC-specific T cell clones (TCC), and significantly lower MDSCs. Similar correlations between clinical response and CD8 T cell density, CD8/Treg and CD8/CD4 ratios were observed in a clinical trial of PD-1 inhibition in NSCLC *(43)*. In addition, the number of NSCLC-specific T cell clones was found to be correlated with tumor mutational burden *(53)*, which is a known predictive biomarker for immune checkpoint inhibition in NSCLC *(54)*. Next, we divided virtual patients into 5 subgroups with increasing level of each biomarker and calculated the ORR of each subgroup. Figure 7 confirmed that ORR increased as the biomarkers identified above increased (or decreased in case of MDSC). However, the disease control rate, which is defined as percentage of patients with complete/partial response and stable disease, increases only when CD8/Treg, CD8/CD4, and TCC increase or when MDSC decreases.

To study the combined effect of the predictive biomarkers, we trained a random forest model using pre-treatment CD8/4 T cells, PD-L1 expression, CD8/Treg, CD8/CD4 ratios, MDSC density, and TCC (see Methods). As a prerequisite, we calculated the correlation matrix to make sure that the variables were not strongly correlated (Supplementary Figure 5A). The variable importance of all pre-treatment biomarkers is shown in Supplementary Figure 6A, with CD8/Treg ratio, PD-L1 expression, CD8 density, and TCC

10

identified as top important variables by the random forest model. With ROC analysis, we selected
thresholds for the four predictive biomarkers that achieved a sensitivity of 80% (Figure 8A). The
thresholds for CD8/Treg ratio, PD-L1 expression, CD8 density, and TCC were 4.1, 21%, 151 cells/mm^2,
and 72 (with specificity of 47%, 35%, 37%, and 34%), respectively. Here, we converted the CD8 density
from 3-D to 2-D that corresponds to the outcome of digital pathology analysis *(26)*. Further, we
performed similar analyses on on-treatment biomarkers. We selected CD8/Treg ratio and CD8 density at
the end of first treatment cycle (day 14), which were identified by the random forest model as the two
most important variables (Supplementary Figure 5B and 6B). The thresholds, according to ROC analysis
in Figure 8B, were selected to be 5.1 and 176 cells/mm^2 (with specificity of 52% and 41%). Overall,
CD8/Treg ratio showed the best performance with the highest specificity and area under ROC curve
(Figure 8). In comparison, Kim et al. analyzed tumor-infiltrating lymphocytes in 33 primary lung lesions
from advanced NSCLC and found that a Treg/CD8 ratio cutoff of 0.25 achieved a sensitivity and
specificity of 82.6% and 65.4% in predicting response to anti-PD-1 treatment *(43)*. In a meta-analysis, Li
et al. also identified tumor PD-L1 expression and mutational burden as predictive biomarkers (both with
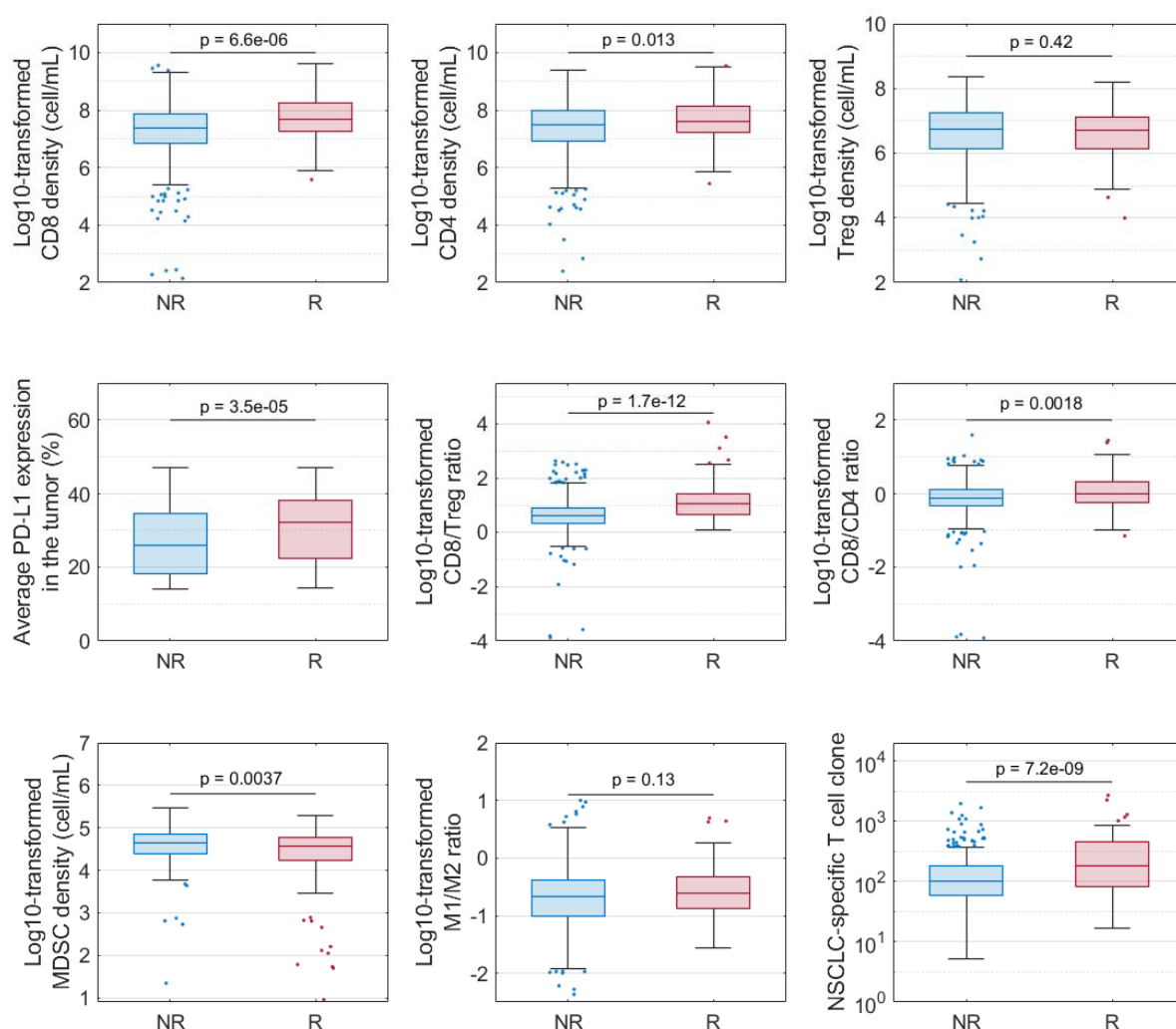specificity of about 30% when sensitivity is 80%) for anti-PD-(L)1 treatment in NSCLC *(55, 56)*.

Figure 6. Comparison of pre-treatment variable distributions between responders (R) and non-responders (NR). p-values were calculated by Wilcoxon test.
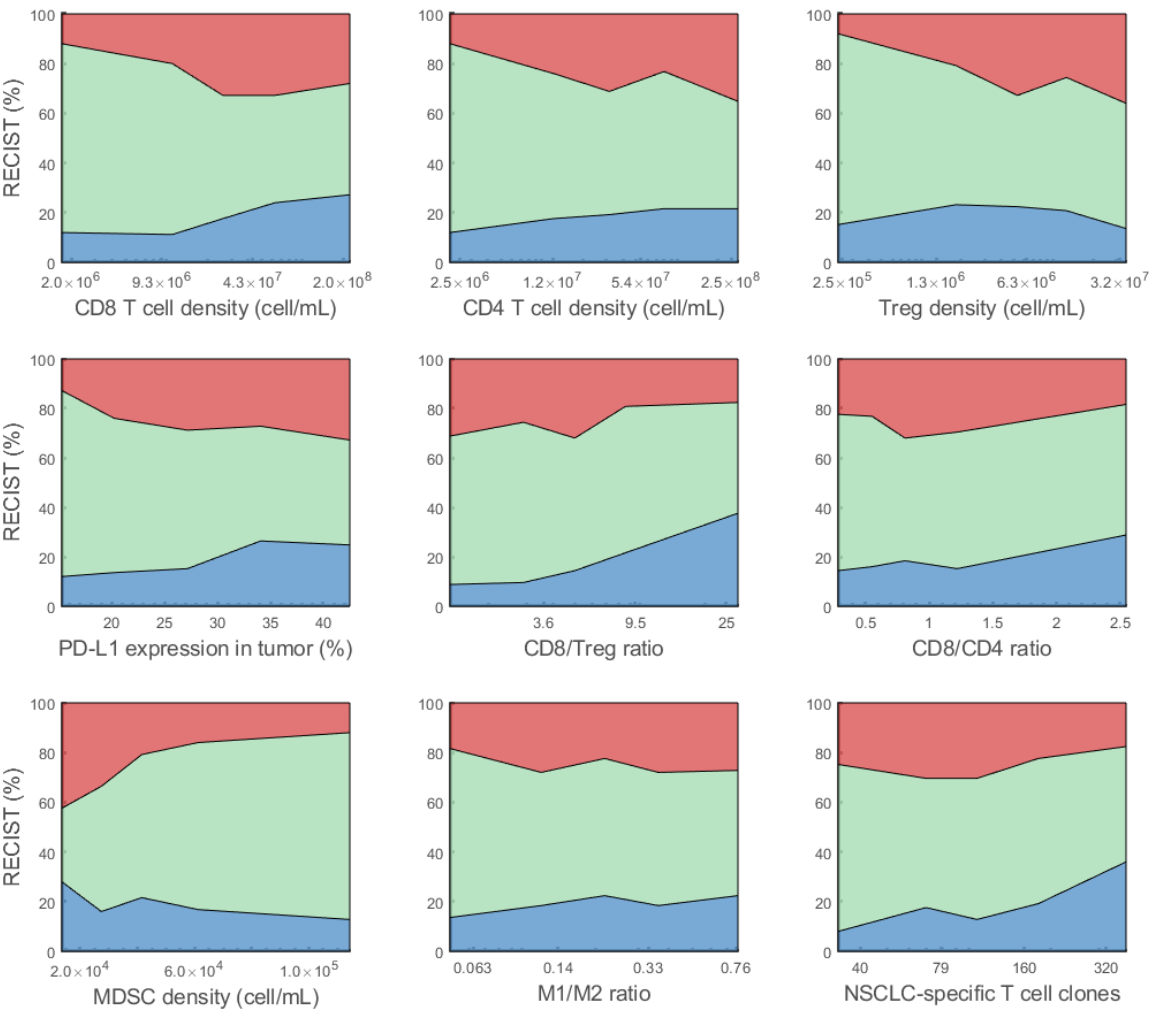
11

304

Figure 7. Effect of pre-treatment variables on objective response. For each variable of interest, virtual patients are sorted by the variable amount in ascending order, and evenly divided into 5 subgroups. The response status of each subgroup is plotted against the corresponding median variable amount. Blue represents partial or complete response. Green represents stable disease. Red represents progressive disease.
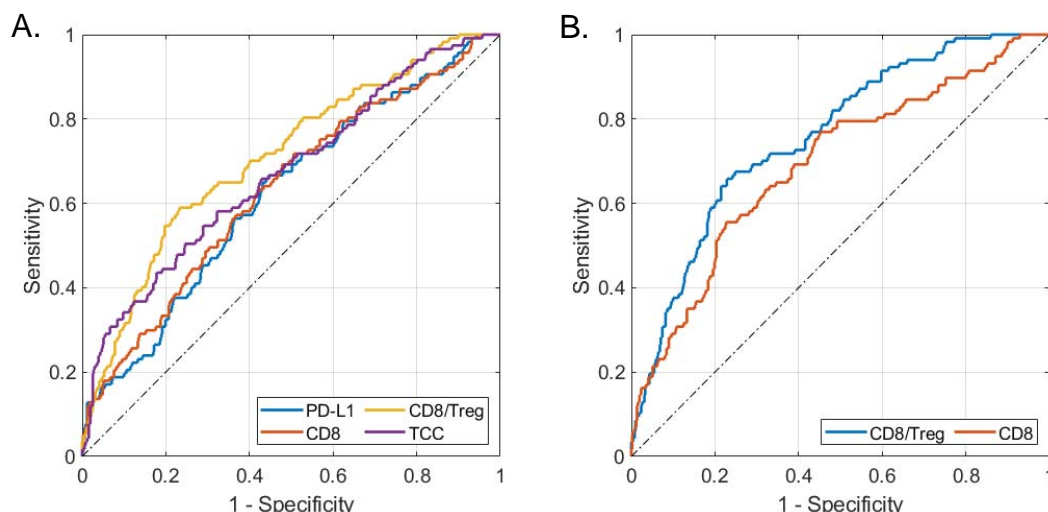
Figure 8. ROC analysis of (A) pre-treatment and (B) on-treatment predictive biomarkers for PD-L1 inhibition in NSCLC. Areas under curve (auROC) were 0.62, 0.63, 0.71, 0.67 for pre-treatment PD-L1 expression, CD8 T cell density, CD8/Treg ratio, and NSCLC-specific T cell clones (TCC), respectively; auROC were 0.76 and 0.69 for on-treatment CD8/Treg ratio and CD8 density at the end of first treatment cycle (day 14).

To explore dynamics of immune cells during immunotherapy, we visualized the time-dependent profiles of immune cells in the central (Supplementary Figure 7) and tumor compartment (Supplementary Figure 8). Supplementary Figure 7 shows that all activated T cell subsets in blood, including CD8, CD4, helper T cells, and Tregs were increased by durvalumab in responders, while CD8/Treg and CD8/CD4 ratios decreased over time in responders. On the contrary, immune cells in the non-responders had opposite dynamics when compared to the responders. For immune cells in the tumor, Supplementary Figure 8 shows that activated T cell subsets also increased in responders during PD-L1 inhibition. However, unlike T cell ratios in blood, CD8/CD4 ratio increased in responders, and CD8/Treg ratio was transiently increased by durvalumab in responders for the first two months and did not drastically change from the baseline level in the long term. Furthermore, M1/M2 ratio decreased and MDSC density increased in responders, suggesting that TAMs and MDSC may partly contribute to resistance to immunotherapy in NSCLC *(57)*. Sensitivity analysis (Supplementary Figure 9) also suggested that recruitment of MDSC, Th-to-Treg differentiation, and M2 polarization could be potential targets of drugs that can be combined with durvalumab, as parameters related to these mechanisms were among the most influential ones to tumor size at the end of durvalumab treatment.

DISCUSSION

In the present study, we revisited PD-(L)1 simulation in NSCLC with the latest QSP model expansion and attempted to address the challenge on generating heterogeneous yet physiologically realistic virtual patients, which was raised in our previous studies *(13–15)*. In terms of model structure, we utilized previously developed QSP model of TNBC and incorporated an additional source of IFNγ in the tumor microenvironment (see Methods). In addition, baseline values of cancer type-specific parameters were recalibrated by experimental and clinical data on stage III NSCLC. Notably, PD-L1 in the model represents the average expression on all tumor cells, including cancer cells and immune cells, that can interact with PD-1 on activated T cells and TAMs to inhibit Teff-mediated cancer killing and TAM-mediated phagocytosis. However, PD-L1 on different cell types may have different roles in the tumor microenvironment *(58)*, and thus can be separately modeled in future studies. In addition, PD-L1 expression is upregulated only by IFNγ in the current model, so we assume a baseline PD-L1 expression

13

348 to match the percentage of virtual patients in the PD-L1-high and PD-L1-low groups as observed in the
349 clinical trial. It should be noted that multiple inflammatory signaling pathways are involved in PD-L1
350 upregulation, which results in the clinically observed heterogeneous PD-L1 expression *(59)*. Additional
351 mechanistic details can be incorporated into the model when sufficient experimental data become
352 available for model calibration.

354 One of our main focuses is to improve our approach to virtual patient generation. In previous studies, we
355 randomly generated deviations around baseline parameter values assuming uniform, log-uniform, or log-
356 normal distribution, and manually calibrated the distribution statistics (e.g., standard deviation, upper and
357 lower boundaries) so that the summary statistics in virtual patients matched those reported by clinical
358 analyses *(15)*. This is a time-consuming process, which becomes even more challenging when fitting to
359 multi-dimensional data. The probability of inclusion proposed by Allen et al. allowed us to select virtual
360 patients that statistically matched the observed data from the randomly generated plausible patients *(21)*,
361 and iAtlas portal provided cancer-specific patient-level data for this method. However, unlike the model
362 of cholesterol metabolism presented by Allen et al., physiologically plausible ranges for the present QSP
363 model variables are not well established due to the insufficient biological understanding of the tumor
364 microenvironment. Therefore, we could not apply the additional step to optimize plausible patients via
365 simulated annealing before calculating the probability of inclusion, which would further improve
366 confidence in model predictions by constraining virtual patients within the physiologically reasonable
367 ranges *(21)*. Comparing to the results from Allen et al., similar proportion (2-3%) of plausible patients in
368 this study was included in the final virtual patient cohort, which depended on the data dimensionality and
369 the initial distribution of plausible patients *(21, 60)*.

371 Besides the three immune subset ratios that were used to select virtual patients in the present analysis
372 (Figure 2), there are other patient characteristics, such as cancer cell growth rate, T cell clonality, and
373 binding affinity between neoantigen and MHC molecules, which also differ among patients but cannot be
374 directly obtained from the immunogenomic data. In future analyses, machine learning algorithms can be
375 applied on multi-omics data to predict model-related parameter values *(61–63)*. Importantly, we have
376 demonstrated here that the virtual patients generated by the QSP model and selected by the three immune
377 subset ratios were able to capture the inter-patient heterogeneity while being consistent with unseen
378 digital pathology data on immune cell densities in NSCLC tumor.

380 To account for variability in PK of durvalumab and predict its intratumoral concentration, we fitted PK
381 parameters in the QSP model to the data simulated from the time-dependent popPK model *(46)* via
382 compressed latent parameterization. This method not only considers the covariance between parameters
383 but also minimizes parameter deviations from the group-average value when there is a lack of parameter
384 identifiability *(23)*. One of the limitations, however, is that the popPK data and the immunogenomic data
385 were collected from two different patient populations, so the covariances between PK-related
386 characteristics and immunogenomic data were not accounted for during virtual patient generation. In
387 addition, as the patient data in iAtlas portal were not body weight dependent, we simulated 750 mg flat
388 dosing instead of weight-based dosing.

390 With the virtual patients that have shown resemblance to real patient data, we investigated if the model
391 could make reliable efficacy prediction for durvalumab in stage III NSCLC. Following the same dose
392 regimen in Study 1108, we simulated 750 mg doses every 2 weeks and divided virtual patients into two
393 subgroups based on their PD-L1 expression on tumor cells. The model predictions fell within the
394 clinically reported confidence intervals and confirmed that patients with high PD-L1 expression have a
395 higher ORR than the PD-L1-low group. It should be noted that appearance of new lesions (e.g.,
396 locoregional and distant metastases) is not a rare event especially during treatment of late-stage NSCLC
397 *(24, 64)*, which would be categorized as progressive disease regardless of the tumor size change. New
398 lesions are most likely seeded before therapy begins and grow to a detectable size during the treatment

399 *(65, 66)*. This stochastic process, which may require a hybrid modeling technique or approximation
400 methods to integrate into the QSP model *(67, 68)*, may be addressed if relevant data become available in
401 the future.
402
403
404 **MATERIALS AND METHODS**

405 **Overview of the QSP modeling platform for immuno-oncology (QSP-IO)**

406 The QSP model comprises four main compartments: central (C), peripheral (P), tumor (T), and tumor-
407 draining lymph node (LN). These compartments represent the circulating blood, lumped peripheral
408 tissues/organs, tumor microenvironment, and lumped tumor-draining lymph nodes, respectively. Ten
409 modules were involved in this study, which described dynamics of cancer cells, T cells (i.e., effector,
410 helper, and regulatory T cells), antigen-presenting cells, neo/self-antigens, therapeutic agent, immune
411 checkpoints, myeloid-derived suppressor cells (MDSCs), and tumor-associated macrophages (TAMs).
412 Cancer type-specific parameters were reparametrized to NSCLC based on experimental data,
413 preferentially from stage III NSCLC if available (Table 1). In addition, we modified our previous
414 assumption so that the main source of interferon-gamma (IFNγ) was not limited to activated CD4 helper
415 T cells. Instead, we assumed that activated CD8 T cells also produced IFNγ with a rate 3 times higher
416 than CD4 T cells *(69)*. For cancer cell growth, we assumed logistic growth for NSCLC with a constant
417 maximum carry capacity of 10 cm (Table 1). Other mechanisms remained the same as in our previous
418 analysis, which was elaborated in *(15)*.
419
420 Overall, there are 255 parameters, 141 ODEs, and 40 algebraic equations (model rules with repeated
421 assignments). Model simulations were performed using SimBiology Toolbox in MATLAB R2020b
422 (Mathworks, Natick, MA) with ODE solver, SUNDIALS. Each simulation started from a single cancer
423 cell, and tumor volume was calculated at each time step via Equation 1. C_{total}, T_{total}, and M_{total} are the
424 total number of cancer cells, T cells, and TAMs; V_{cell}, V_{Tcell}, and V_{Mcell} are volumes of single cancer cell,
425 T cell, and macrophage; C_x and T_{exh} are the numbers of dying cancer cells and exhausted T cells; and
426 $V_{e,T}$ is the volume fraction of intracellular space in NSCLC tumor. During postprocessing, tumor diameter
427 was estimated assuming a spherical tumor.
428

$$V_T = \frac{1}{V_e}(V_{cell}(C_{total} + C_x) + V_{Tcell}(T_{total} + T_{exh}) + V_{Mcell}M_{total})$$

429 (Equation 1)
430
431 **Virtual patient generation**

432 To account for interindividual variability that results in the heterogeneous tumor response to
433 immunotherapy, we selected 30 out of the 255 model parameters, which are known to differ among
434 patients, and generated random deviations around their baseline values using Latin-hypercube sampling
435 (LHS). The distribution statistics (e.g., standard deviation, upper and lower boundaries) were estimated
436 based on available clinical observations and experimental data on NSCLC. In theory, each randomly
437 generated parameter set represents a virtual patient *(70)*. However, to avoid confusion, we define the
438 virtual patients generated at this step as plausible patients. Notably, each patient was randomly assigned a
439 preset initial tumor diameter (see *initial_tumour_size* in Table 1) *(40, 41)*. When the tumor size reached
440 the preset value, the model variables were saved and treated as the pre-treatment characteristics for the
441 corresponding patient. At this step, we generated 30,000 plausible patients.
442
443 To generate a virtual patient cohort whose characteristics statistically match the real patient population,
444 we adapted the probability of inclusion proposed by Allen et al. *(21)*. We first explored the "Immune Cell
445 Proportions" data from the "Immune Feature Trends" module in iAtlas portal (https://isb-

446   cgc.shinyapps.io/shiny-iatlas/) by selecting TGCA subtypes: lung adenocarcinoma (LUAD) and lung
447   squamous cell carcinoma (LUSC), which are the two major subtypes of NSCLC *(22, 71)*. Then, we
448   downloaded the proportions of CD8, CD4, and regulatory T cell (Treg), M1 and M2 macrophages from
449   analyses of the two TCGA subtypes; and we generated a 3-dimensional patient-level data containing
450   ratios between CD8 T cells and Tregs, CD8 and CD4 T cells, and M1 and M2 macrophages, all of which
451   have corresponding QSP model species. Data points that contained zero value(s) were removed to avoid
452   singularities. Moreover, as the TCGA data were collected from untreated patients, they correspond to the
453   pre-treatment characteristics predicted by the model *(72)*. Finally, we calculated the probability of
454   inclusion via Equation 2, which is the conditional probability of including a plausible patient into the final
455   virtual patient cohort (i.e., $S(\theta) = 1$) given the model prediction $M(\theta) = r$.
456

$$P(S(\theta) = 1 | M(\theta) = r) = \beta \frac{\rho_{obs}(r)}{\rho_{sim}(r)}$$

457   (Equation 2)
458
459   Here, S is a logical function that equals to 1 if the plausible patient θ should be included and 0 if
460   otherwise, and M represents the QSP model that predicts time-dependent profile of model variables for
461   the plausible patient θ. In this study, we focused on the model-predicted pre-treatment ratios that
462   corresponded to the data from iAtlas (i.e., CD8/Treg, CD8/CD4, and M1/M2). Additionally, $\rho_{obs}(r)$ and
463     $\rho_{sim}(r)$ are the probability density estimate for model-predicted ratios, r, in the observed data and the
464   plausible patients, respectively. Probability densities were estimated by $\rho(r) = \frac{N}{V_N(r)}$ where $V_N(r)$ is the
465   volume of an N-dimensional hypersphere with radius defined by the distance to the N-th nearest-neighbor
466   of r. N was typically chosen from 5 to 10 in this study. The constant β was optimized by the simulated
467   annealing algorithm to minimize the average two-sample Kolmogorov-Smirnov test statistic when
468   evaluating the difference between the empirical cumulative distribution functions of the observed data
469   from real patients and the predicted values from selected virtual patients *(21)*. With the optimal β, virtual
470   patients were selected based on the inclusion probability to generate the final virtual patient cohort.
471

472   **In silico clinical trial**

473   To account for the interindividual variability in pharmacokinetics of durvalumab, we applied compressed
474   latent parameterization proposed by Tivay et al. *(23)* to generate PK parameters for the virtual patients.
475   Since this method required patient-level PK data for durvalumab, which were not available from
476   published studies, we first generated time-dependent durvalumab PK of 400 pseudo-patients based on the
477   population PK (popPK) study by Baverel et al. *(46)*. Specifically, we assumed log-normal distribution for
478   patient characteristics, such as serum albumin level, body weight, and soluble PD-L1 level, and we
479   estimated the standard deviations based on the reported means and ranges. For categorical variables,
480   including sex and Eastern Cooperative Oncology Group (ECOG) performance status, we assumed
481   binomial distribution with probabilities estimated by the summary statistics of corresponding patient
482   characteristics. Based on the estimated distributions, we randomly generated characteristics of 400
483   pseudo-patients and calculated values for linear clearance, Cl, maximum elimination rate, V_{max}, and
484   volumes of the two compartments, V_1 and V_2, in the popPK model using algebraic equations provided by
485   Baverel et al. *(46)*. Intercompartmental clearance, Q, was assumed to be 0.476 L/day for all patients.
486   Since time-dependent profile of the patient characteristics were not available, we assumed they were
487   constant over time. With the following ODEs for the two-compartment popPK model, we simulated the
488   durvalumab concentration profile in the 400 pseudo-patients *(46)*.
489

$$V_1 \frac{d}{dt}[A]_1 = Q \cdot ([A]_2 - [A]_1) - Cl \cdot [A]_1 - V_{max} \frac{[A]_1}{[A]_1 + K_m}$$

490   (Equation 3)

$$V_2 \frac{d}{dt}[A]_2 = Q \cdot ([A]_1 - [A]_2)$$

491   (Equation 4)
492
493   The first step of compressed latent parameterization is to find the "group-average" model defined by
494    $\bar{\theta} = \arg\min_\theta \left\| \mathbf{Y} - \hat{\mathbf{Y}}(\theta) \right\|_2^2$, where $\mathbf{Y}$ is a matrix storing data from all patients and $\hat{\mathbf{Y}}(\theta)$ is the
495   corresponding model predictions *(23)*. Here, due to the high variability in durvalumab PK, we defined $\mathbf{Y}$
496   as an Nt-by-1 vector storing the median durvalumab concentration in the 400 pseudo-patients at each time
497   point (Nt is the length of the time vector), and $\hat{\mathbf{Y}}(\theta)$ as an another Nt-by-1 vector storing the QSP model-
498   predicted durvalumab concentration given an input PK parameter set θ. We fitted six PK parameters,
499   which were capillary filtration rate, blood volume, volume fraction of interstitial space in peripheral
500   tissues available to durvalumab, linear and maximum non-linear clearance rates, and Michaelis-Menten
501   constant for non-linear clearance, using MATLAB function, fmincon. Then, we randomly generated
502   k=500 random local deviations around the group-average model, which was stored in a 6-by-k matrix $\mathbf{\Theta}$.
503   The corresponding changes in model-predicted serum durvalumab concentration were stored in a Nt-by-k
504   vector $\hat{\mathbf{Y}}_\mathbf{\Theta}$. Through singular value decomposition of the covariance matrix $\mathbf{C} = \hat{\mathbf{Y}}_\mathbf{\Theta} \mathbf{\Theta}^T = \mathbf{USV}^T$, we got a
505   6-by-6 matrix $\mathbf{V}$ whose columns are sorted orthogonal directions of maximum covariance in the parameter
506   space *(23)*. Further, we fitted the six PK parameters in the QSP model to the pseudo-patient data
507   generated above via $\theta_i = \arg\min_\theta \left\| Y_i - \hat{Y}(\theta) \right\|_2^2 + \lambda \left\| (\theta - \bar{\theta})^T \mathbf{V} \right\|_1$, and a latent parameter space was
508   constructed via $\mathbf{\phi}^T = \mathbf{\theta}^T \mathbf{V} - \bar{\theta}^T \mathbf{V}$, where $\mathbf{\theta}$ is a 6-by-400 matrix storing all fitted parameter sets. Finally,
509   new PK parameter sets were randomly generated from the latent space via $\theta_{VP_i} = \mathbf{V}\phi_i + \bar{\theta}$ for the virtual
510   patients, where the 6-by-1 vector ϕ_i was randomly sampled from the latent space $\mathbf{\phi}$ assuming
511   independent uniform distribution for each dimension of the latent parameter space.
512
513   With the final virtual patient cohort, we simulated their tumor response to durvalumab treatment starting
514   from the time point when the tumors reached their preset initial diameter (i.e., pre-treatment tumor size),
515   following the same settings in a phase 1/2 clinical trial of durvalumab (NCT01693562) *(24)*. 10 mg/kg
516   durvalumab was administered every 2 weeks (Q2W) via a SimBiology dose object. Tumor diameters
517   were recorded at 6, 12, and 16 weeks, and every 8 weeks thereafter, corresponding to the frequency of
518   pre-scheduled tumor size measurement in the clinical trial. Clinical response was classified by RECIST
519   v1.1 *(73)* with a minimum duration of stable disease of 6 weeks.
520
521   **Statistical analyses**
522   For comparison between model-predicted ORRs and clinical observation, bootstrap sampling was
523   performed to resample the virtual patient (sub)population with a sample size matching the number of
524   patients in the corresponding subgroups (i.e., PD-L1 high/low) in Study 1108. The bootstrap median and
525   the 95 percentile confidence intervals were then calculated. Wilcoxon tests were conducted using
526   ranksum function in MATLAB 2020b.
527
528   Random forest models were trained on potential predictive biomarkers of interest to predict response
529   status using caret and randomForest packages in R 4.2.3. For each model, 500 trees were trained, and
530   each tree was trained on two-thirds of the data points. The out-of-bag error is defined as the error rate of
531   each tree in predicting the data excluded by the training set (i.e., out-of-bag samples). The Mean Decrease
532   Accuracy for each variable is the average decrease of model accuracy in predicting outcomes of the out-
533   of-bag samples when a particular variable is excluded from the model, which is reported as variable
534   importance. Receiver Operating Characteristic (ROC) analyses were performed by perfcurve function in
535   MATLAB 2020b.
536

17

537 Sensitivity analysis was performed using Morris screening/elementary effects method *(74, 75)* with a 11-
538 level grid and a step size Δ of 1/10 for the 30-dimensional hypercube $[0,1]^{30}$ (i.e., 30 input parameters
539 varied during virtual patient generation). Actual values of the 30 parameters were calculated based on
540 their distributions by treating the sampled points from the hypercube as quantiles *(75)*. 1000 trajectories
541 were randomly generated at the beginning. Trajectories with points fell outside the hypercube, as well as
542 those with points containing 0% and 100% quantiles for parameters with lognormal distribution, were
543 disregarded. Overall, 34 successful trajectories were plugged into the model to simulate tumor sizes at
544 day 400 of durvalumab treatment, which were used to calculate the elementary effects (EEs). Finally, the
545 variance σ^2 and the mean absolute values μ^* of the EEs were estimated for each parameter *(75)*.
546

566 **References**

567 1. R. L. Siegel, K. D. Miller, H. E. Fuchs, A. Jemal, Cancer statistics, 2022. *CA A Cancer J Clinicians* **72**,
568 7–33 (2022).

569 2. A. K. Ganti, A. B. Klein, I. Cotarla, B. Seal, E. Chou, Update of Incidence, Prevalence, Survival, and
570 Initial Treatment in Patients With Non–Small Cell Lung Cancer in the US. *JAMA Oncol* **7**, 1824 (2021).

571 3. M. D. Shields, J. A. Marin-Acevedo, B. Pellini, Immunotherapy for Advanced Non–Small Cell Lung
572 Cancer: A Decade of Progress. *American Society of Clinical Oncology Educational Book* , e105–e127
573 (2021).

574 4. K. Chen, G. Cheng, F. Zhang, G. Zhu, Y. Xu, X. Yu, Z. Huang, Y. Fan, PD-L1 expression and T cells
575 infiltration in patients with uncommon EGFR-mutant non-small cell lung cancer and the response to
576 immunotherapy. *Lung Cancer* **142**, 98–105 (2020).

577 5. M. Nakamura, S. Kageyama, S. Niho, M. Okumura, H. Hojo, A. Motegi, N. Nakamura, S. Zenda, K.
578 Yoh, K. Goto, T. Akimoto, Impact of EGFR Mutation and ALK Translocation on Recurrence Pattern
579 After Definitive Chemoradiotherapy for Inoperable Stage III Non-squamous Non–small-cell Lung Cancer.
580 *Clinical Lung Cancer* **20**, e256–e264 (2019).

581   6. M. Chevallier, M. Borgeaud, A. Addeo, A. Friedlaender, Oncogenic driver mutations in non-small cell
582   lung cancer: Past, present and future. *WJCO* **12**, 217–237 (2021).

583   7. T. A. Leil, S. Ermakov, Editorial: The emerging discipline of quantitative systems pharmacology.
584   *Front. Pharmacol.* **6** (2015), doi:10.3389/fphar.2015.00129.

585   8. S. S. Aghamiri, R. Amin, T. Helikar, Recent applications of quantitative systems pharmacology and
586   machine learning models across diseases. *J Pharmacokinet Pharmacodyn* **49**, 19–37 (2022).

587   9. V. Chelliah, P. H. van der Graaf, Model□informed target identification and validation through
588   combining quantitative systems pharmacology with network□based analysis. *CPT Pharmacom & Syst*
589   *Pharma* **11**, 399–402 (2022).

590   10. J. P. F. Bai, J. C. Earp, J. Florian, R. Madabushi, D. G. Strauss, Y. Wang, H. Zhu, Quantitative
591   systems pharmacology: Landscape analysis of regulatory submissions to the US Food and Drug
592   Administration. *CPT Pharmacom & Syst Pharma* **10**, 1479–1484 (2021).

593   11. M. Jafarnejad, C. Gong, E. Gabrielson, I. H. Bartelink, P. Vicini, B. Wang, R. Narwal, L. Roskos, A.
594   S. Popel, A Computational Model of Neoadjuvant PD-1 Inhibition in Non-Small Cell Lung Cancer. *AAPS*
595   *J* **21**, 79 (2019).

596   12. R. J. Sové, M. Jafarnejad, C. Zhao, H. Wang, H. Ma, A. S. Popel, QSP-IO: A Quantitative Systems
597   Pharmacology Toolbox for Mechanistic Multiscale Modeling for Immuno-Oncology Applications. *CPT*
598   *Pharmacometrics Syst Pharmacol* **9**, 484–497 (2020).

599   13. H. Wang, H. Ma, R. J. Sové, L. A. Emens, A. S. Popel, Quantitative systems pharmacology model
600   predictions for efficacy of atezolizumab and nab-paclitaxel in triple-negative breast cancer. *J Immunother*
601   *Cancer* **9**, e002100 (2021).

602   14. H. Wang, R. J. Sové, M. Jafarnejad, S. Rahmeh, E. M. Jaffee, V. Stearns, E. T. Roussos Torres, R. M.
603   Connolly, A. S. Popel, Conducting a Virtual Clinical Trial in HER2-Negative Breast Cancer Using a
604   Quantitative Systems Pharmacology Model With an Epigenetic Modulator and Immune Checkpoint
605   Inhibitors. *Front Bioeng Biotechnol* **8**, 141 (2020).

606   15. H. Wang, C. Zhao, C. A. Santa-Maria, L. A. Emens, A. S. Popel, Dynamics of tumor-associated
607   macrophages in a quantitative systems pharmacology model of immunotherapy in triple-negative breast
608   cancer. *iScience* **25**, 104702 (2022).

609   16. H. Ma, H. Wang, R. J. Sové, J. Wang, C. Giragossian, A. S. Popel, Combination therapy with T cell
610   engager and PD-L1 blockade enhances the antitumor potency of T cells as predicted by a QSP model. *J*
611   *Immunother Cancer* **8** (2020), doi:10.1136/jitc-2020-001141.

612   17. H. Ma, H. Wang, R. J. Sove, M. Jafarnejad, C.-H. Tsai, J. Wang, C. Giragossian, A. S. Popel, A
613   Quantitative Systems Pharmacology Model of T Cell Engager Applied to Solid Tumor. *AAPS J* **22**, 85
614   (2020).

615   18. R. J. Sové, B. K. Verma, H. Wang, W. J. Ho, M. Yarchoan, A. S. Popel, Virtual clinical trials of anti-
616   PD-1 and anti-CTLA-4 immunotherapy in advanced hepatocellular carcinoma using a quantitative
617   systems pharmacology model. *J Immunother Cancer* **10**, e005414 (2022).

618   19. G. Lazarou, V. Chelliah, B. G. Small, M. Walker, P. H. van der Graaf, A. M. Kierzek, Integration of
619   Omics Data Sources to Inform Mechanistic Modeling of Immune-Oncology Therapies: A Tutorial for
620   Clinical Pharmacologists. *Clin Pharmacol Ther* **107**, 858–870 (2020).

621   20. V. Chelliah, G. Lazarou, S. Bhatnagar, J. P. Gibbs, M. Nijsen, A. Ray, B. Stoll, R. A. Thompson, A.
622   Gulati, S. Soukharev, A. Yamada, J. Weddell, H. Sayama, M. Oishi, S. Wittemer-Rump, C. Patel, C.
623   Niederalt, R. Burghaus, C. Scheerans, J. Lippert, S. Kabilan, I. Kareva, N. Belousova, A. Rolfe, A. Zutshi,
624   M. Chenel, F. Venezia, S. Fouliard, H. Oberwittler, A. Scholer-Dahirel, H. Lelievre, D. Bottino, S. C.
625   Collins, H. Q. Nguyen, H. Wang, T. Yoneyama, A. Z. X. Zhu, P. H. van der Graaf, A. M. Kierzek,
626   Quantitative Systems Pharmacology Approaches for Immuno-Oncology: Adding Virtual Patients to the
627   Development Paradigm. *Clin Pharmacol Ther* **109**, 605–618 (2021).

628   21. R. Allen, T. Rieger, C. Musante, Efficient Generation and Selection of Virtual Populations in
629   Quantitative Systems Pharmacology Models. *CPT Pharmacometrics Syst. Pharmacol.* **5**, 140–146 (2016).

630   22. J. A. Eddy, V. Thorsson, A. E. Lamb, D. L. Gibbs, C. Heimann, J. X. Yu, V. Chung, Y. Chae, K.
631   Dang, B. G. Vincent, I. Shmulevich, J. Guinney, CRI iAtlas: an interactive portal for immuno-oncology
632   research. *F1000Res* **9**, 1028 (2020).

633   23. A. Tivay, G. C. Kramer, J.-O. Hahn, in *2020 American Control Conference (ACC)*, (IEEE, Denver,
634   CO, USA, 2020), pp. 1335–1340.

635   24. S. J. Antonia, A. Balmanoukian, J. Brahmer, S.-H. I. Ou, M. D. Hellmann, S.-W. Kim, M.-J. Ahn, D.-
636   W. Kim, M. Gutierrez, S. V. Liu, P. Schöffski, D. Jäger, R. Jamal, G. Jerusalem, J. Lutzky, J. Nemunaitis,
637   L. Calabrò, J. Weiss, S. Gadgeel, J. Bhosle, P. A. Ascierto, M. C. Rebelatto, R. Narwal, M. Liang, F.
638   Xiao, J. Antal, S. Abdullah, N. Angra, A. K. Gupta, S. N. Khleif, N. H. Segal, Clinical Activity,
639   Tolerability, and Long-Term Follow-Up of Durvalumab in Patients With Advanced NSCLC. *J Thorac*
640   *Oncol* **14**, 1794–1806 (2019).

641   25. Y. Van Herck, A. Antoranz, M. D. Andhari, G. Milli, O. Bechter, F. De Smet, F. M. Bosisio,
642   Multiplexed Immunohistochemistry and Digital Pathology as the Foundation for Next-Generation
643   Pathology in Melanoma: Methodological Comparison and Future Clinical Applications. *Front Oncol* **11**,
644   636681 (2021).

645   26. H. Mi, C. Gong, J. Sulam, E. J. Fertig, A. S. Szalay, E. M. Jaffee, V. Stearns, L. A. Emens, A. M.
646   Cimino-Mathews, A. S. Popel, Digital Pathology Analysis Quantifies Spatial Heterogeneity of CD3, CD4,
647   CD8, CD20, and FoxP3 Immune Markers in Triple-Negative Breast Cancer. *Front Physiol* **11**, 583333
648   (2020).

649   27. H. Mi, W. J. Ho, M. Yarchoan, A. S. Popel, Multi-Scale Spatial Analysis of the Tumor
650   Microenvironment Reveals Features of Cabozantinib and Nivolumab Efficacy in Hepatocellular
651   Carcinoma. *Front Immunol* **13**, 892250 (2022).

652   28. H. Mi, S. Sivagnanam, C. B. Betts, S. M. Liudahl, E. M. Jaffee, L. M. Coussens, A. S. Popel,
653   Quantitative Spatial Profiling of Immune Populations in Pancreatic Ductal Adenocarcinoma Reveals
654   Tumor Microenvironment Heterogeneity and Prognostic Biomarkers. *Cancer Res* , CAN-22-1190 (2022).

655   29. A. Ruiz-Martinez, C. Gong, H. Wang, R. J. Sové, H. Mi, H. Kimko, A. S. Popel, Simulations of
656   tumor growth and response to immunotherapy by coupling a spatial agent-based model with a whole-
657   patient quantitative systems pharmacology model. *PLoS Comput Biol* **18**, e1010254 (2022).

658 30. D. S. Chen, I. Mellman, Oncology Meets Immunology: The Cancer-Immunity Cycle. *Immunity* **39**, 1–
659   10 (2013).

660 31. K. Usuda, Y. Saito, M. Sagawa, M. Sato, K. Kanma, S. Takahashi, C. Endo, Y. Chen, A. Sakurada, S.
661   Fujimura, Tumor doubling time and prognostic assessment of patients with primary lung cancer. *Cancer*
662   **74**, 2239–2244 (1994).

663 32. A. J. Synn, W. Li, R. San José Estépar, C. Zhang, G. R. Washko, G. T. O'Connor, T. Araki, H.
664   Hatabu, A. A. Bankier, M. A. Mittleman, M. B. Rice, Radiographic pulmonary vessel volume, lung
665   function and airways disease in the Framingham Heart Study. *Eur Respir J* **54**, 1900408 (2019).

666 33. J. D. Armstrong, E. H. Gluck, R. O. Crapo, H. A. Jones, J. M. Hughes, Lung tissue volume estimated
667   by simultaneous radiographic and helium dilution methods. *Thorax* **37**, 676–679 (1982).

668 34. L. Hlatky, Clinical Application of Antiangiogenic Therapy: Microvessel Density, What It Does and
669   Doesn't Tell Us. *CancerSpectrum Knowledge Environment* **94**, 883–893 (2002).

670 35. H. Zhang, A. S. Verkman, Microfiberoptic Measurement of Extracellular Space Volume in Brain and
671   Tumor Slices Based on Fluorescent Dye Partitioning. *Biophysical Journal* **99**, 1284–1291 (2010).

672 36. X. Zhang, Y. Wang, J. Fan, W. Chen, J. Luan, X. Mei, S. Wang, Y. Li, L. Ye, S. Li, W. Tian, K. Yin,
673   D. Ju, Blocking CD47 efficiently potentiated therapeutic effects of anti-angiogenic therapy in non-small
674   cell lung cancer. *j. immunotherapy cancer* **7**, 346 (2019).

675 37. E. R. Parra, M. C. Ferrufino-Schmidt, A. Tamegnon, J. Zhang, L. Solis, M. Jiang, H. Ibarguen, C.
676   Haymaker, J. J. Lee, C. Bernatchez, I. I. Wistuba, Immuno-profiling and cellular spatial analysis using
677   five immune oncology multiplex immunofluorescence panels for paraffin tumor tissue. *Sci Rep* **11**, 8511
678   (2021).

679 38. T. J. Welsh, R. H. Green, D. Richardson, D. A. Waller, K. J. O'Byrne, P. Bradding, Macrophage and
680   Mast-Cell Invasion of Tumor Cell Islets Confers a Marked Survival Advantage in Non–Small-Cell Lung
681   Cancer. *JCO* **23**, 8959–8967 (2005).

682 39. The Cancer Genome Atlas Research Network, Comprehensive genomic characterization of squamous
683   cell lung cancers. *Nature* **489**, 519–525 (2012).

684 40. A. Rittmeyer, F. Barlesi, D. Waterkamp, K. Park, F. Ciardiello, J. von Pawel, S. M. Gadgeel, T. Hida,
685   D. M. Kowalski, M. C. Dols, D. L. Cortinovis, J. Leach, J. Polikoff, C. Barrios, F. Kabbinavar, O. A.
686   Frontera, F. De Marinis, H. Turna, J.-S. Lee, M. Ballinger, M. Kowanetz, P. He, D. S. Chen, A. Sandler,
687   D. R. Gandara, OAK Study Group, Atezolizumab versus docetaxel in patients with previously treated
688   non-small-cell lung cancer (OAK): a phase 3, open-label, multicentre randomised controlled trial. *Lancet*
689   **389**, 255–265 (2017).

690 41. N. Ghaffari Laleh, C. M. L. Loeffler, J. Grajek, K. Staňková, A. T. Pearson, H. S. Muti, C. Trautwein,
691   H. Enderling, J. Poleszczuk, J. N. Kather, D. A. Lauffenburger, Ed. Classical mathematical models for
692   prediction of response to chemotherapy and immunotherapy. *PLoS Comput Biol* **18**, e1009822 (2022).

693 42. T. K. Kilvaer, E.-E. Paulsen, S. Andersen, M. Rakaee, R. M. Bremnes, L.-T. R. Busund, T. Donnem,
694   Digitally quantified CD8+ cells: the best candidate marker for an immune cell score in non-small cell
695   lung cancer? *Carcinogenesis* **41**, 1671–1681 (2020).

21

696   43. H. Kim, H. J. Kwon, Y. B. Han, S. Y. Park, E. S. Kim, S. H. Kim, Y. J. Kim, J. S. Lee, J.-H. Chung,
697   Increased CD3+ T cells with a low FOXP3+/CD8+ T cell ratio can predict anti-PD-1 therapeutic response
698   in non-small cell lung cancer patients. *Mod Pathol* **32**, 367–375 (2019).

699   44. M. Rakaee, L.-T. R. Busund, S. Jamaly, E.-E. Paulsen, E. Richardsen, S. Andersen, S. Al-Saad, R. M.
700   Bremnes, T. Donnem, T. K. Kilvaer, Prognostic Value of Macrophage Phenotypes in Resectable Non–
701   Small Cell Lung Cancer Assessed by Multiplex Immunohistochemistry. *Neoplasia* **21**, 282–293 (2019).

702   45. X. Zheng, A. Weigert, S. Reu, S. Guenther, S. Mansouri, B. Bassaly, S. Gattenlöhner, F. Grimminger,
703   S. Savai Pullamsetti, W. Seeger, H. Winter, R. Savai, Spatial Density and Distribution of Tumor-
704   Associated Macrophages Predict Survival in Non–Small Cell Lung Carcinoma. *Cancer Research* **80**,
705   4414–4425 (2020).

706   46. P. G. Baverel, V. F. S. Dubois, C. Y. Jin, Y. Zheng, X. Song, X. Jin, P. Mukhopadhyay, A. Gupta, P.
707   A. Dennis, Y. Ben, P. Vicini, L. Roskos, R. Narwal, Population Pharmacokinetics of Durvalumab in
708   Cancer Patients and Association With Longitudinal Biomarkers of Disease Status. *Clin Pharmacol Ther*
709   **103**, 631–642 (2018).

710   47. H. Wang, O. Milberg, I. H. Bartelink, P. Vicini, B. Wang, R. Narwal, L. Roskos, C. A. Santa-Maria,
711   A. S. Popel, In silico simulation of a clinical trial with anti-CTLA-4 and anti-PD-L1 immunotherapies in
712   metastatic breast cancer using a systems pharmacology model. *R Soc Open Sci* **6**, 190366 (2019).

713   48. S. D. Finley, A. S. Popel, Predicting the Effects of Anti-angiogenic Agents Targeting Specific VEGF
714   Isoforms. *AAPS J* **14**, 500–509 (2012).

715   49. US Food and Drug Administration. Clinical pharmacology and biopharmaceutics review(s) for
716   Application number 761069Orig1s000.
717   https://www.accessdata.fda.gov/drugsatfda_docs/nda/2017/761069Orig1s000ClinPharmR.pdf (2016).

718   50. X. Cheng, V. Veverka, A. Radhakrishnan, L. C. Waters, F. W. Muskett, S. H. Morgan, J. Huo, C. Yu,
719   E. J. Evans, A. J. Leslie, M. Griffiths, C. Stubberfield, R. Griffin, A. J. Henry, A. Jansson, J. E. Ladbury,
720   S. Ikemizu, M. D. Carr, S. J. Davis, Structure and interactions of the human programmed cell death 1
721   receptor. *J Biol Chem* **288**, 11771–11785 (2013).

722   51. M. Mkrtichyan, Y. G. Najjar, E. C. Raulfs, L. Liu, S. Langerman, G. Guittard, L. Ozbun, S. N. Khleif,
723   B7-DC-Ig enhances vaccine effect by a novel mechanism dependent on PD-1 expression level on T cell
724   subsets. *J Immunol* **189**, 2338–2347 (2012).

725   52. H. Chen, R. Lin, W. Lin, Q. Chen, D. Ye, J. Li, J. Feng, W. Cheng, M. Zhang, Y. Qi, An immune
726   gene signature to predict prognosis and immunotherapeutic response in lung adenocarcinoma. *Sci Rep* **12**,
727   8230 (2022).

728   53. Q. Jia, W. Wu, Y. Wang, P. B. Alexander, C. Sun, Z. Gong, J.-N. Cheng, H. Sun, Y. Guan, X. Xia, L.
729   Yang, X. Yi, Y. Y. Wan, H. Wang, J. He, P. A. Futreal, Q.-J. Li, B. Zhu, Local mutational diversity
730   drives intratumoral immune heterogeneity in non-small cell lung cancer. *Nat Commun* **9**, 5361 (2018).

731   54. M. Yarchoan, A. Hopkins, E. M. Jaffee, Tumor Mutational Burden and Response Rate to PD-1
732   Inhibition. *N Engl J Med* **377**, 2500–2501 (2017).

733 55. Y. Li, Z. Chen, W. Tao, N. Sun, J. He, Tumor mutation score is more powerful than tumor mutation
734 burden in predicting response to immunotherapy in non-small cell lung cancer. *Cancer Immunol*
735 *Immunother* **70**, 2367–2378 (2021).

736 56. H. J. An, H. J. Chon, C. Kim, Peripheral Blood-Based Biomarkers for Immune Checkpoint Inhibitors.
737 *IJMS* **22**, 9414 (2021).

738 57. S. Peters, L. Paz-Ares, R. S. Herbst, M. Reck, Addressing CPI resistance in NSCLC: targeting TAM
739 receptors to modulate the tumor microenvironment and future prospects. *J Immunother Cancer* **10**,
740 e004863 (2022).

741 58. N. Patsoukis, Q. Wang, L. Strauss, V. A. Boussiotis, Revisiting the PD-1 pathway. *Sci. Adv.* **6**,
742 eabd2712 (2020).

743 59. M. Yi, M. Niu, L. Xu, S. Luo, K. Wu, Regulation of PD-L1 expression in the tumor
744 microenvironment. *J Hematol Oncol* **14**, 10 (2021).

745 60. T. R. Rieger, R. J. Allen, C. J. Musante, Modeling is data driven: Use it for successful virtual patient
746 generation. *CPT Pharmacometrics Syst Pharmacol* **10**, 393–394 (2021).

747 61. C. H. Lee, M. Salio, G. Napolitani, G. Ogg, A. Simmons, H. Koohy, Predicting Cross-Reactivity and
748 Antigen Specificity of T Cell Receptors. *Front Immunol* **11**, 565096 (2020).

749 62. R. You, W. Qu, H. Mamitsuka, S. Zhu, DeepMHCII: a novel binding core-aware deep interaction
750 model for accurate MHC-II peptide binding affinity prediction. *Bioinformatics* **38**, i220–i228 (2022).

751 63. D. J. Cook, J. Kallus, R. Jörnsten, J. Nielsen, Molecular natural history of breast cancer: Leveraging
752 transcriptomics to predict breast cancer progression and aggressiveness. *Cancer Med* **9**, 3551–3562
753 (2020).

754 64. D. König, S. Schär, D. Vuong, M. Guckenberger, K. Furrer, I. Opitz, W. Weder, S. I. Rothschild, A.
755 Ochsenbein, A. Zippelius, A. Addeo, M. Mark, E. I. Eboulet, S. Hayoz, S. Thierstein, D. C. Betticher, H.-
756 B. Ris, R. Stupp, A. Curioni-Fontecedro, S. Peters, M. Pless, M. Früh, Long-term outcomes of operable
757 stage III NSCLC in the pre-immunotherapy era: results from a pooled analysis of the SAKK 16/96,
758 SAKK 16/00, SAKK 16/01, and SAKK 16/08 trials. *ESMO Open* **7**, 100455 (2022).

759 65. E. D. Yorke, Z. Fuks, L. Norton, W. Whitmore, C. C. Ling, Modeling the development of metastases
760 from primary and locally recurrent tumors: comparison with a clinical data base for prostatic cancer.
761 *Cancer Res* **53**, 2987–2993 (1993).

762 66. H. Imai, R. Onozato, K. Kaira, S. Kawashima, K. Masubuchi, T. Nagashima, K. Tajima, K. Minato,
763 Course of postoperative relapse in non-small cell lung cancer is strongly associated with post-progression
764 survival. *Thorac Cancer* **12**, 2740–2748 (2021).

765 67. K. N. Yamamoto, L. L. Liu, A. Nakamura, H. Haeno, F. Michor, Stochastic Evolution of Pancreatic
766 Cancer Metastases During Logistic Clonal Expansion. *JCO Clinical Cancer Informatics* , 1–11 (2019).

767 68. D. A. Cruz, M. L. Kemp, Hybrid computational modeling methods for systems biology. *Prog. Biomed.*
768 *Eng.* **4**, 012002 (2022).

769   69. T. Kasahara, J. J. Hooks, S. F. Dougherty, J. J. Oppenheim, Interleukin 2-mediated immune interferon
770   (IFN-gamma) production by human T cells and T cell subsets. *J Immunol* **130**, 1784–1789 (1983).

771   70. Y. Cheng, R. Straube, A. E. Alnaif, L. Huang, T. A. Leil, B. J. Schmidt, Virtual Populations for
772   Quantitative Systems Pharmacology Models. *Methods Mol Biol* **2486**, 129–179 (2022).

773   71. V. Thorsson, D. L. Gibbs, S. D. Brown, D. Wolf, D. S. Bortone, T.-H. Ou Yang, E. Porta-Pardo, G. F.
774   Gao, C. L. Plaisier, J. A. Eddy, E. Ziv, A. C. Culhane, E. O. Paull, I. K. A. Sivakumar, A. J. Gentles, R.
775   Malhotra, F. Farshidfar, A. Colaprico, J. S. Parker, L. E. Mose, N. S. Vo, J. Liu, Y. Liu, J. Rader, V.
776   Dhankani, S. M. Reynolds, R. Bowlby, A. Califano, A. D. Cherniack, D. Anastassiou, D. Bedognetti, Y.
777   Mokrab, A. M. Newman, A. Rao, K. Chen, A. Krasnitz, H. Hu, T. M. Malta, H. Noushmehr, C. S.
778   Pedamallu, S. Bullman, A. I. Ojesina, A. Lamb, W. Zhou, H. Shen, T. K. Choueiri, J. N. Weinstein, J.
779   Guinney, J. Saltz, R. A. Holt, C. S. Rabkin, Cancer Genome Atlas Research Network, A. J. Lazar, J. S.
780   Serody, E. G. Demicco, M. L. Disis, B. G. Vincent, I. Shmulevich, The Immune Landscape of Cancer.
781   *Immunity* **48**, 812-830.e14 (2018).

782   72. The Cancer Genome Atlas Research Network, Comprehensive molecular profiling of lung
783   adenocarcinoma. *Nature* **511**, 543–550 (2014).

784   73. E. A. Eisenhauer, P. Therasse, J. Bogaerts, L. H. Schwartz, D. Sargent, R. Ford, J. Dancey, S. Arbuck,
785   S. Gwyther, M. Mooney, L. Rubinstein, L. Shankar, L. Dodd, R. Kaplan, D. Lacombe, J. Verweij, New
786   response evaluation criteria in solid tumours: revised RECIST guideline (version 1.1). *Eur J Cancer* **45**,
787   228–247 (2009).

788   74. M. T. Wentworth, R. C. Smith, H. T. Banks, Parameter Selection and Verification Techniques Based
789   on Global Sensitivity Analysis Illustrated for an HIV Model. *SIAM/ASA J. Uncertainty Quantification* **4**,
790   266–297 (2016).

791   75. A. Saltelli, M. Ratto, T. Andres, F. Campolongo, J. Cariboni, D. Gatelli, M. Saisana, S. Tarantola,
792   *Global Sensitivity Analysis. The Primer* (John Wiley & Sons, Ltd, Chichester, UK, 2007;
793   http://doi.wiley.com/10.1002/9780470725184).